# Observations of the North Polar Region of Mars from the Mars Orbiter Laser Altimeter

Maria T. Zuber*, David E. Smith, Sean C. Solomon,
James B. Abshire, Robert S. Afzal, Oded Aharonson,
Kathryn Fishbaugh, Peter G. Ford, Herbert V. Frey,
James B. Garvin, James W. Head, Anton B. Ivanov,
Catherine L. Johnson, Duane O. Muhleman, Gregory A. Neumann,
Gordon H. Pettengill, Roger J. Phillips, Xiaoli Sun, H. Jay Zwally,
W. Bruce Banerdt, Thomas C. Duxbury

Elevations from the Mars Orbiter Laser Altimeter (MOLA) have been used to construct a precise topographic map of the martian north polar region. The northern ice cap has a maximum elevation of 3 kilometers above its surroundings but lies within a 5-kilometer-deep hemispheric depression that is contiguous with the area into which most outflow channels emptied. Polar cap topography displays evidence of modification by ablation, flow, and wind and is consistent with a primarily $H_2O$ composition. Correlation of topography with images suggests that the cap was more spatially extensive in the past. The cap volume of $1.2 \times 10^6$ to $1.7 \times 10^6$ cubic kilometers is about half that of the Greenland ice cap. Clouds observed over the polar cap are likely composed of $CO_2$ that condensed out of the atmosphere during northern hemisphere winter. Many clouds exhibit dynamical structure likely caused by the interaction of propagating wave fronts with surface topography.

The north polar ice cap of Mars is one of the largest present-day reservoirs of volatiles on that planet and preserves the record of seasonal cycles of carbon dioxide and dust (1–4). Measurements of polar cap topography furnish critical constraints on volatile abundance and composition and provide a quantitative basis for studying surface-atmosphere interactions relevant to present and past hydrological cycles. Since arrival at Mars on 12 September 1997, the Mars Orbiter laser altimeter (MOLA) (5, 6), an instrument on the Mars Global Surveyor (MGS) spacecraft (7), has collected ~2.6 million measurements of

M. T. Zuber, O. Aharonson, G. A. Neumann, and G. H. Pettengill are in the Department of Earth, Atmospheric, and Planetary Sciences, Massachusetts Institute of Technology, Cambridge, MA 02139, USA. D. E. Smith, J. B. Abshire, R. S. Afzal, J. B. Garvin, H. V. Frey, G. A. Neumann, X. Sun, M. T. Zuber, and H. J. Zwally are at the Earth Sciences Directorate, NASA/Goddard Space Flight Center, Greenbelt, MD 20771, USA. P. G. Ford is at the Center for Space Research, Massachusetts Institute of Technology, Cambridge, MA 02139, USA. K. Fishbaugh and J. W. Head are in the Department of Geological Sciences, Brown University, Providence, RI 02912, USA. A. B. Ivanov and D. O. Muhleman are at the California Institute of Technology, Pasadena, CA 91125, USA. R. J. Phillips is in the Department of Earth and Planetary Sciences, Washington University, St. Louis, MO 63130, USA. C. L. Johnson and S. C. Solomon are in the Department of Terrestrial Magnetism, Carnegie Institution of Washington, Washington D.C. 20015, USA. W. B. Banerdt and T. C. Duxbury are at the Jet Propulsion Laboratory, Pasadena, CA 91109.

*To whom correspondence should be addressed: zuber@tharsis.gsfc.nasa.gov

topography and cloud heights in the northern hemisphere of Mars (8). These observations afford a new view of martian polar processes that has broad implications for the planet's seasonal and climatic evolution.

MOLA coverage (Fig. 1) includes profiles across Mars's northern hemisphere collected during three spacecraft orbital phases (9): the aerobraking hiatus orbit (AHO; 18 profiles) and science phasing orbits (SPO) before and after Mars solar conjunction in May 1997 (SPO-1 and 2; 61 and 127 profiles). The MOLA instrument operates with maximum signal/noise ratio and minimum range error when oriented at a 0° incidence angle with respect to the martian surface. However, when ranging in this nadir-oriented configuration, the inclination of the MGS orbit (~93.7°) resulted in an ~450-km-diameter gap in coverage, centered on the pole. In order to obtain measurements of topography at latitudes above 86.3°N, the MGS spacecraft was pointed ~50° off-nadir on alternate passes during 2 weeks in June and July 1998. Ten profiles were collected in this mode, which enabled the maximum height of the ice cap to be measured.

Several major geologic units are located in the high-latitude northern hemisphere of Mars (Fig. 1A). Polar deposits consist of layered terrain and residual ice (Apl and Api); the residual ice constitutes the perennial ice deposits, which are distinguished from seasonal frosts. Circumpolar deposits consist of a variety of types of mantled plains (Hv), outliers of residual ice that may mark the former extent of polar ice (Api), and a range of surface dune deposits (Adl and Adc).

Previous regional topographic measurements of the martian north polar cap were based on stereo imaging and three Mariner 9 radio occultation measurements (10, 11). These results suggested that the northern cap rose 4 to 6 km above the surroundings and had two maxima in elevation located at approximately 88°N, 120°E and 83°N, 10°E. The MOLA observations have much higher spatial sampling and provide an increase in vertical accuracy of ~2 orders of magnitude over previous measurements. The new observations reveal a different topographic expression of the ice cap and surroundings.

**Regional setting and the hydrological cycle.** As shown in a 2-km grid (Fig. 1B) of northern hemisphere topography (12), the elevation of the north polar cap increases progressively toward the pole from its southern limit at ~80°N. The highest point of the polar cap is within a few kilometers of the rotation pole and has an elevation of –1950 ± 50 m with respect to the average elevation of the equator (13). The terrain that surrounds the ice cap lies between –4800 and –5200 m, leading to a cap relief of approximately 2950 ± 200 m. The root-mean-square misfit of elevations of the 10 profiles that cross the north pole is 28 m.

The martian surface outside the ice cap slopes gently downward toward the pole at all longitudes in the northern hemisphere (for example, Fig. 2) and most steeply in the vicinity of the Tharsis rise. Thus, except within the bounds of the 1500-km-diameter circular depression centered at 45°N, 110°E in Utopia Planitia (14), any liquid water will flow to high northern latitudes. Most previous studies have assumed that transport of water between the polar caps and crust occurs almost solely by insolation-driven exchange between the surface and the atmosphere (15, 16). However, the topography in Fig. 2 suggests that water could potentially have flowed overland or beneath the surface to the martian north pole.

Clifford (17) proposed that a global-scale sub-permafrost groundwater system may have facilitated transport of $H_2O$ from the north pole to the equator on Mars. In this model, basal melting of the polar cap due to pressure loading and the local thermal gradient produces a downward percolation of groundwater into a global aquifer. For reasonable values of crustal permeability and for the assumed elevation based on earlier data, the hydrostatic head associated with the groundwater beneath the cap could have driven $10^8$ $km^3$ of groundwater to the equator over martian history, a volume that would represent an important contribution to the

long-term cycling of water (*17*). However, the MOLA data show that the base of the polar cap is 5 km below the mean equatorial level, and so a significantly larger hydrostatic head than previously thought would be required to transport $H_2O$ to the equator by this mechanism. The difference in elevation between the equator and the north pole, combined with other factors such as frictional head loss and energy balance (*18*), would appear to diminish or eliminate the potential contribution of a hemispheric-scale subsurface aquifer system to the long-term climatic cycling of water on Mars. However, if the formation of the areally extensive Tharsis rise (<70°N; 210° to 295°E in Fig. 1B) produced global-scale changes in Mars's gravitational potential (*19*), then regional topographic lows and fluid transport paths on early Mars may have been different from those indicated in Fig. 1B.

**Layered terrain**. Layered ice deposits (mapped in Fig. 1A) represent the most dis-tinctive component of the north polar cap (*1*). The layered terrains lie atop plains units and form the permanent ice cap. Topographic profiles across the ice cap (for example, Fig. 3) show that the martian surface rises sharply by about 1000 m at the edge of the layered deposits, in comparison to the ~2000 m rise estimated previously (*10*). Thin, alternating bright and dark bands observed at the margin of the cap probably preserve the record of seasonal and climatic deposition of ice and dust. Topographic profiles do not show steps that correlate with individual layers at the edge of the cap. The lack of correlation of the topography with individual layers is not surprising given recent images by the Mars Orbiter camera (*20*) that show evidence for multiple layering at scales of <10 m (the limit of resolution of the camera) over spatial baselines of several kilometers.

A 1-km grid of polar topography (Fig. 4) shows that large areas of the top of the permanent ice cap are smooth; regional slopes over many tens of kilometers are approximately 0.2°. In several areas topography has been observed to be smooth at the sub-meter resolution of the instrument (*21*) over spatial scales of kilometers. For example, the "stair-step" structures in Fig. 5 show that surfaces are flat over spatial scales of ~1.2 km and have ~2 m vertical offsets on longer baselines.

**Troughs and chasms**. Figures 3 and 4 show that the ice cap is cut by canyons and spiral troughs, analogs of which do not occur on any glacial or polar terrain on Earth (*1*). These structures cut the upper portions of the layered deposits to depths below the surface as great as 1 km; some penetrate to nearly the level of surrounding terrain. The interiors of chasms exhibit lower values of 1.064-$\mu$m-wavelength reflectivity than the nearby terrain, which indicates that these structures are sinks for windblown dust (*6*). In the present state, down-slope wind flow from the cap tends to spiral westward to about 80°N because of Coriolis forcing (*22*), but the troughs trend to the east. Therefore troughs cannot be
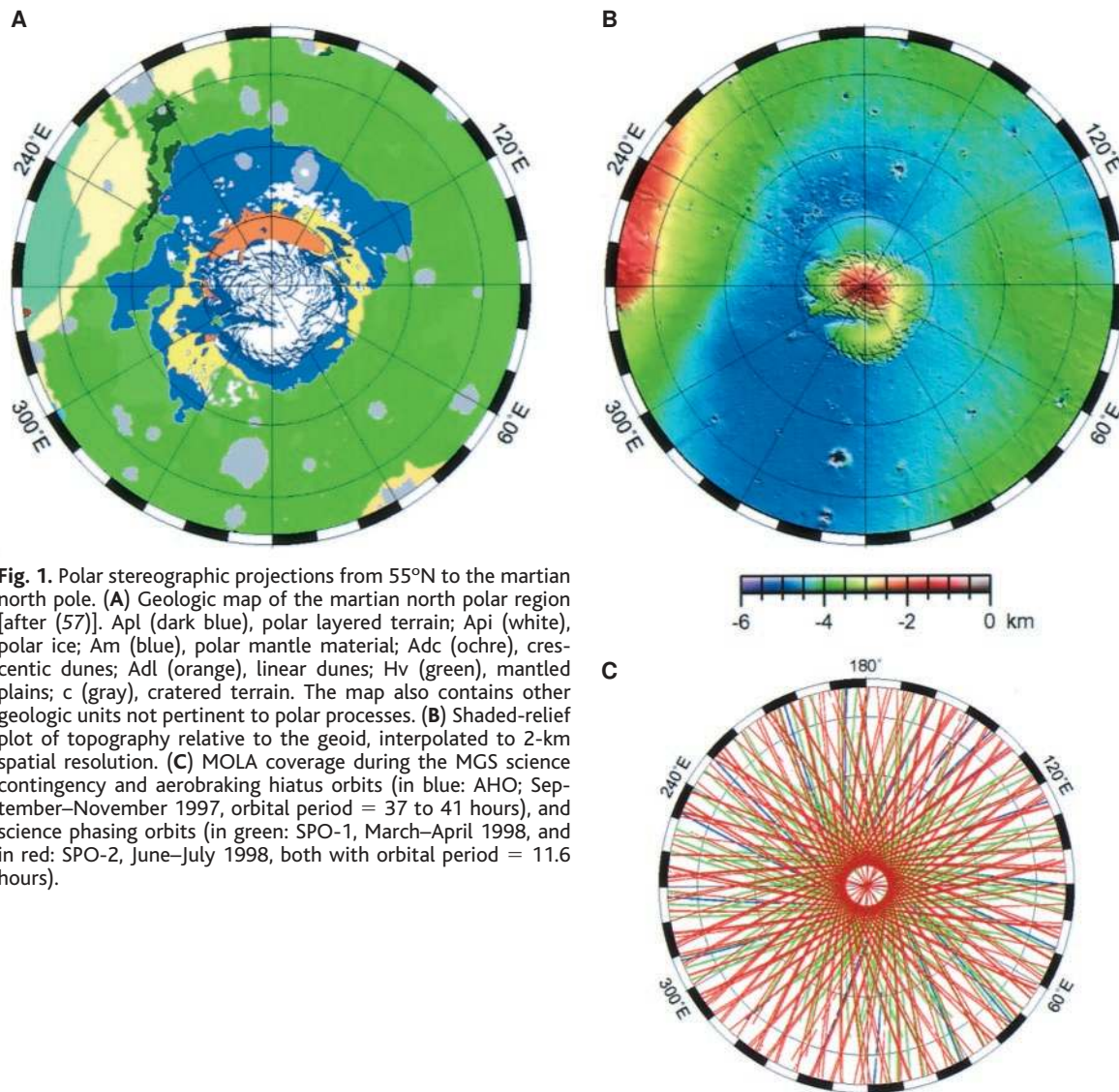


**Fig. 1.** Polar stereographic projections from 55°N to the martian north pole. (**A**) Geologic map of the martian north polar region [after (*57*)]. Apl (dark blue), polar layered terrain; Api (white), polar ice; Am (blue), polar mantle material; Adc (ochre), crescentic dunes; Adl (orange), linear dunes; Hv (green), mantled plains; c (gray), cratered terrain. The map also contains other geologic units not pertinent to polar processes. (**B**) Shaded-relief plot of topography relative to the geoid, interpolated to 2-km spatial resolution. (**C**) MOLA coverage during the MGS science contingency and aerobraking hiatus orbits (in blue: AHO; September–November 1997, orbital period = 37 to 41 hours), and science phasing orbits (in green: SPO-1, March–April 1998, and in red: SPO-2, June–July 1998, both with orbital period = 11.6 hours).

explained solely by ablation associated with downslope winds. Additional factors, such as the position of the sun, may be required to explain trough formation. With continued ablation the chasms are believed to migrate toward the pole (23, 24).

Chasma Boreale is the large reentrant into the northern polar cap at longitude 300°E. The feature is about 350 km wide at its entrance and 600 km long. It was suggested (25) to have formed by catastrophic discharge of a subglacial volume of meltwater at the base of a polar ice sheet. An alternative interpretation (26) is that the structure formed by erosion as a result of the concentration of down-slope winds. The orientation of this structure is favorable for a combination of downslope winds modified by the Coriolis force as a mechanism for erosion. MOLA elevations provide additional guidance for distinguishing between mechanisms of origin. Figure 6 shows that the relief of the chasm is ~1.5 km from the floor at its headwall to the plateau encompassing the southern lobe of the cap. The floor of Chasma Boreale extends as a tongue southward from the mouth of the reentrant about 50 km and is bounded by a steep scarp that drops about 250 m to the plains below. About 100 km to the south of the mouth of the reentrant is a mesa with about 500 m of relief. An impact crater on the mesa has part of its ejecta blanket removed by the scarp bounding the mesa. If the mesa is genetically linked to Chasma Boreale, then the tongue cannot be a primary depositional feature, as it sits about 400 m beneath the mesa. An alternative possibility is that polar layered deposits once extended as far south as the mesa. Aeolian erosion of polar layered deposits appears to be associated with steep scarps (1) and is a reasonable explanation of the steep boundaries of the mesa and the tongue. The floor of the chasm shows considerable relief, but there is obviously not a monotonic increase in the elevation of the floor in the direction of the headwall. If this surface is of fluvial

origin, then scouring must have taken place all along the channel. We suggest that the present physiography of the floor of Chasma Boreale has been shaped by aeolian processes and is characterized by deflation basins (20) that collect dark dune material.

**Olympia Planitia**. Dunes in the north polar region cover ~700,000 km². The most spatially extensive dune-covered area is Olympia Planitia, a fan-shaped region detached from the main cap at 80°–85°N, 140°–240°E. Previous topography data depicted this area to be a flat plain, but MOLA data show that the region slopes upward toward the pole (Figs. 4 and 7). Figure 7 shows that regional topographic slopes are subtle (~0.15°), but the surface is locally much rougher. This region is covered by straight-crested transverse dunes (27) with average heights of 24 ± 9 m and crest-to-crest spacing of 2.4 ± 1.3 km, although many of the profiles are aliased because MOLA's along-track sample interval is greater than the dune wavelength. We estimate that the sediment volume in the dunes is 10,000 ± 3000 km³. Given limits on the thickness of the underlying basal dust layer (28) the maximum dune volume does not exceed 15,000 km³.

**Outliers**. An additional characteristic of this region is the presence of outliers of the residual polar cap deposit (unit Api in Fig. 1A). Mapped in a band from 75° to 82°N and ~140° to 255°E, these deposits, an example of which is the mesa in Fig. 6, lie in the lowest parts of the circumpolar region in this area and are generally surrounded by mantled smooth plains (Hv). MOLA profiles across polar residual ice remnants reveal that most of these remnants are tens of kilometers across and show prominent positive topography, from tens of meters to over 1000 m.

The large areal extent and topographic prominence of these deposits implies that they are not seasonal and supports the idea that they represent remnants of previous polar cap deposits. Their concentration in a narrow latitudinal arc further supports the idea that they might represent a residual band of polar ice. In addition, the concentration in this area of a wide variety of irregular depressions (Fig. 1B) suggests that zones may be present where residual ice melted or sublimed.

**Impact craters**. MOLA sampled over 100 impact craters in the north polar region, of which over 30 profiles were sufficiently close to the centers of the craters to provide

geometric measurements relevant to understanding the nature of impact mechanics, target properties, and the history of surface modification. Virtually all craters within 100 km of the permanent ice cap display a level of cavity fill beyond that which can be explained by typical structural uplift or interior modification processes such as cavity wall slumping or impact melt ponding. Figure 8A shows a highly infilled 32-km-diameter impact feature located ~50 km from the edge of the north polar cap. The geometry of this structure compared with typical non-polar region craters (Fig. 8B) indicates that ~70% of the initial crater cavity has been infilled. Other impact features adjacent to the permanent cap show even greater fractions of interior deposits. In general, those impact features nearest the edge of the permanent polar cap contain the greatest fraction of fill. These data support the interpretation that cavities of these impact features have been filled by non–impact-related material, such as ice or dust or as a result of a previous polar cap advance.

**Ice cap composition and controls on morphology**. The slopes along the cap periphery and in the spiral troughs are too steep (15° to 20°, occasionally up to 45°) to be a consequence of steady-state flow, which indicates that ablation must be controlling these aspects of morphology. At any local point on the surface of Mars, $CO_2$ frost condenses onto the surface when the temperature is <150 K. When the surface temperature exceeds that value the frost rapidly sublimes back into the atmosphere, likely exposing water ice over the north polar region (29). During northern summer temperatures as high as 205 K have been observed, and the water ice also sublimes into the atmosphere (30). Warm parts of the northern cap undergo ablation, particularly on south-facing slopes, causing these to be steeper than north-facing slopes (Fig. 3). As northern winter approaches, water vapor condenses out onto the ice cap, initially nearest the pole, but eventually over the entire north polar region throughout the winter (31).

A simple radiative model (31, 32) demonstrates that the southern edge of the cap is expected to recede poleward as water is lost to the atmosphere, reaching the extent and shape of the current cap in a little more than $10^6$ martian years. The detailed shapes of the dark troughs can also be explained by the model; a small (2%) decrease in albedo at a
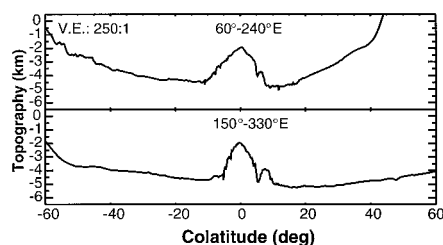


**Fig. 2.** Perpendicular profiles across the north pole of Mars sampled at the stated longitudes from a 2-km grid of MOLA elevations. Note that the north polar region represents a hemispheric minimum in elevation. The Tharsis rise is the topographic high at the right of the top profile. In both profiles, the higher longitude is on the right. Vertical exaggeration (V.E.) is 250:1.
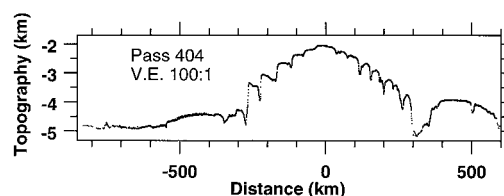


**Fig. 3.** Pass 404, which crossed directly over the north pole, shows that the polar cap has a maximum elevation of about 3 km above its surroundings. Vertical exaggeration (V.E.) is 100:1.

given latitude will create a deep trough in less than $10^6$ years. The shape of the ice cap and details of the trough produced by the model fit the MOLA data well.

It had been thought that viscoplastic flow has not played a role in shaping ice cap topography, on the basis of the absence of evidence of faults or filled crevasses at layer deposit exposures (11) and Viking images showing constant thicknesses in exposed horizontal layers (1). However, recent experimental data (33) on ice rheology at north polar pressures and temperatures indicate that the north polar cap should flow. Strain rate scales with the exponential of temperature, so flow velocities will be greater in periods of high obliquity, and also in summer as compared to winter. Figure 5 shows that the surface of the ice cap is smooth (on the scale of the laser footprint) at the submeter scale over baselines of hundreds of

meters to kilometers. Over baselines of tens of kilometers, surfaces that do not contain troughs are typically smooth at the 10-m level (Fig. 4). In ice caps, short wavelength (much less than the ice thickness) undulations are damped in the surface of a flowing ice cover (34). Smooth or gently undulating surface topography is thus characteristic of thick ice that has undergone flow, although wind erosion as a contributor to topographic smoothness cannot be ruled out. In addition, a MOC image of the northern cap (20) shows that some exposed layers vary in thickness in a manner that could be interpreted as a result of flow deformation.

The azimuthal topography of the north polar cap is variable, but the broadscale planform of the topography in several longitude ranges is consistent with that expected for viscous flow (35). Application of a model that balances accumulation with outward

flow (36) produces a predicted topography that fits the MOLA profiles best for negligible accumulation rates and slow radial flow velocities (<1 mm per martian year) for $H_2O$ ice rheology (33). Carbon dioxide, the major constituent of the martian atmosphere and the component that exchanges with the cap over the course of the seasons, is rheologically too weak (37) to explain the observed planform of the permanent cap. Temperature has the same functional dependence on flow as that of mixed particulates (38), so flow modeling cannot be used to estimate dust fraction unless the temperature is well known.

The time scales for ablation are shorter than for flow, but during periods of larger obliquity flow may have been enhanced. In recent times ablation must have dominated the shaping of the northern cap particularly with regard to troughs and chasms. Deformation due to viscous flow is currently minimal, and the evidence for this process may be preserved from an earlier warmer period.

**Former extent of the residual cap**. On the basis of the topography of Olympia Planitia and the presence of the ring of residual ice patches in the mantled plains adjacent to it,
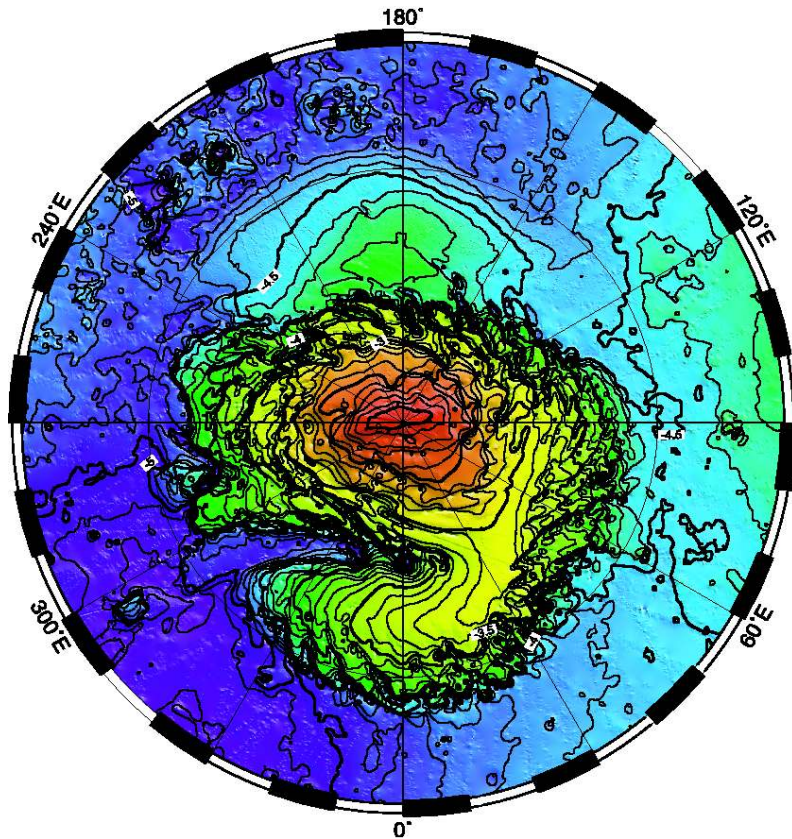


**Fig. 4.** Polar projection of MOLA topography between 75°N and the north pole interpolated to 1-km spatial resolution. The contour interval is 100 m. The absolute accuracy of grid points with respect to Mars's center of mass is ranges from 5 to 30 m. The figure was constructed using software from (58).



**Fig. 5.** Pass 210 shows 4 s of data centered at 85.7°N, 4.0°E, corresponding to a 15-km distance along the MGS spacecraft groundtrack. The shot spacing is 400 m. Gray lines show that the maximum along-track slope is 0.2° and the minimum slope is statistically indistinguishable from 0° over a 1.6 km baseline. This profile demonstrates that over smooth surfaces the instrument is performing at its 37.5-cm range resolution. Vertical exaggeration (V.E.) is 90:1.
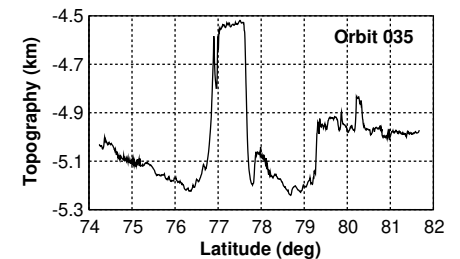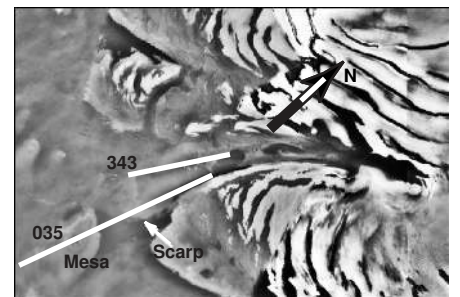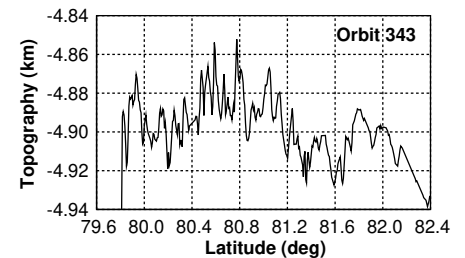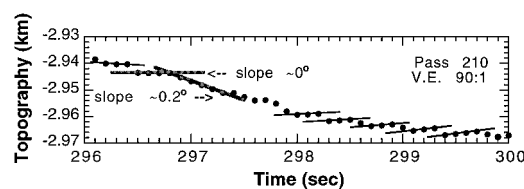


**Fig. 6.** Viking image mosaic of Chasma Boreale showing MOLA elevations along Passes 35 and 343. Pass 343 shows a scarp at the mouth of Chasma Boreale on left (south) end of the profile and a basin (filled with dark dune material) on the right (north) end. Pass 35 shows a scarp and an outlier mesa and crosses an impact crater on the mesa.

we propose that the material underlying the longitudinal dunes in Olympia Planitia is an extension of the polar cap deposits and that the patches of residual ice ringing this region represent remnants of the former extent of the polar cap. Additional evidence to support this conclusion is that the outer edge of these deposits and the currently exposed continuous residual ice deposits extend symmetrically in an arc around the present north rotational pole. The continuation of several spiral troughs from the residual cap into Olympic

Planitia is also consistent with this interpretation. In addition, the presence of a crater in the dunes that has a topographic signature similar to others at high latitudes not in dune units supports the contention that the dunes likely represent a carapace of sediments that overlie buried ice. The cause of the present configuration of deposits is not known, but it may be related to volatile loss or preferential ponding of dust, perhaps as a result of the low topography of the adjacent north polar basin. Olympia Planitia is also geometrically similar

to the part of the residual cap south of Chasma Boreale (longitude range 315° to 30°E), which further suggests that the dune-covered region may once have been part of the main cap.

The close proximity of the circumpolar deposits to the polar deposits and the evidence cited above for the former greater lateral extent of the polar deposits suggests that the modification and erosion of previous polar deposits was an important source of sediments currently observed in the circumpolar mantling deposits (*39*).

**Volume**. The volume of the permanent ice deposits provides an important limit on the present-day $H_2O$ abundance on Mars. Estimating volume requires knowledge of basement topography, which for terrestrial ice sheets is determined from radar sounding (*40*). Such information is not available for Mars. One simple estimate of the cap volume has been made by interpolating a topographic surface under the cap and then subtracting this inferred basement topography from the measured topography (*41*). If the coincidence of the topographic levels of the floor of the deepest chasm (Boreale) and the surrounding circumpolar terrain means that the floor of this chasm lies at the base of the cap, then this geometric approach should be a reasonable first approximation. Using this geometric method, we estimate that the north polar cap is $1.2 \pm 0.2 \times 10^6$ km$^3$ over an area of $1.04 \times 10^6$ km$^2$, for an average thickness of 1030 m. Our uncertainty in the volume estimate includes a few tens of meters of average error in the top surface and a few hundred meters average error in the interpolated basal surface, but both the estimate and its uncertainty ignore the possibility of lithospheric flexure if the possibility of (see below). Surface dunes represent less than 1% of the cap volume and so are insignificant within the bounds of uncertainty. The estimated ice volume corresponds to an equivalent global layer of water 9 m deep. If the north polar cap melted, the estimated volume would fill to approximately the −4680 m contour and cover a region of $4.5 \times 10^6$ km$^2$. The average water depth would be 270 m. The southernmost extent of the melted cap would be in the Chryse Basin (~45°N, 340°E), which coincides with the area into which most outflow channels emptied (*42*). It has been proposed (*43*) that the northern lowlands were occupied by a large standing body of water derived from these channels in the past. The volume of the polar cap estimated above is about an order of magnitude less than the volume derived from MOLA data (*39*) for the area below the youngest proposed shoreline (*43*).

For comparison, in Greenland the grounded ice volume is $2.99 \times 10^6$ km$^3$ in an area of $1.67 \times 10^6$ km$^2$, and the average thickness is



**Fig. 7.** Pass 247 shows a topographic profile across the residual cap (at left) and Olympia Planitia. Vertical exaggeration (V.E.) is 38:1.
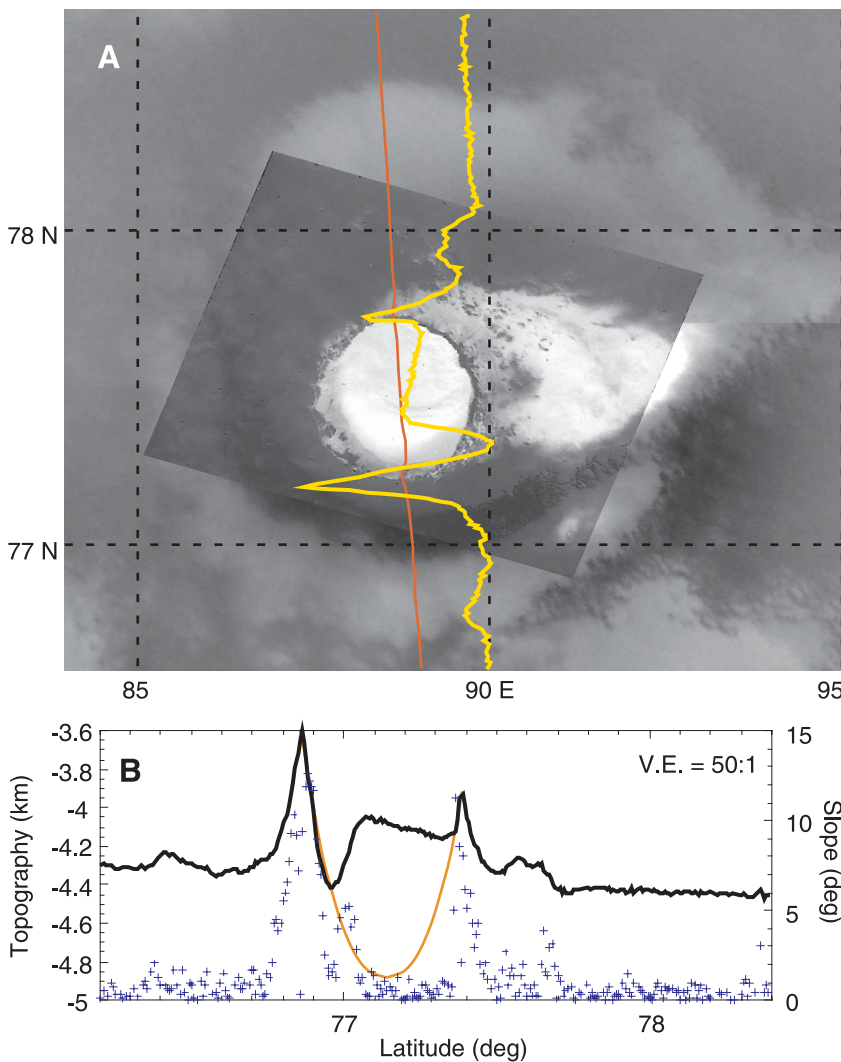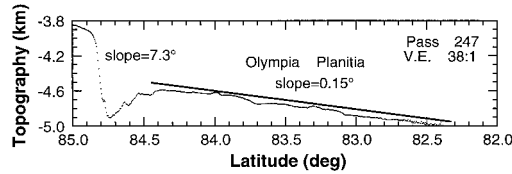


**Fig. 8. (A)** Viking image 65B58 (resolution 52 m pixel$^{-1}$) of a ~30-km-diameter ice-filled impact crater at 77°N, 215°E. Shown are the MGS groundtrack and MOLA elevations along Pass 415. **(B)** Cross-sectional view of profile with MOLA elevations and shot-to-shot surface slopes (plus symbols), plotted versus latitude. The parabolic line is the reconstructed crater cavity based upon MOLA observations of non-polar craters (*59*). Vertical exaggeration (V.E.) is 50:1.

1.79 km (*44*). The error in the volume estimate is approximately ±10%. In Antarctica, the grounded ice volume is $29.3 \pm 2.5 \times 10^6$ km$^3$ in an area of $12.0 \times 10^6$ km$^2$, and the average thickness is 2.44 km (*40*). Floating ice shelves yield an additional $0.7 \times 10^6$ km$^3$. Although the volume of the martian polar cap has a greater uncertainty than these terrestrial measurements because of the need to estimate basal topography, the surface elevation of the martian north cap is now known, on average, better than parts of Greenland and Antarctica. Gridded elevations from terrestrial radar altimetry range from about 1-m accuracy in flatter portions to 50 to 100 m near margins, and areas not covered by satellite radar altimetry (latitudes >82°S) are known only to within ~100 m (*45*). If the polar ice cap is approximately $10^6$ km$^3$ in volume and has an average density of 1000 kg m$^{-3}$, approximately equivalent to water ice, then the mass of cap material is approximately $10^{18}$ kg.

If the martian ice cap is isostatically uncompensated, then a mass of $10^{18}$ kg distributed over $10^6$ km$^2$ will cause a gravity anomaly of ~50 mGal. Pre-MGS gravity models (*46, 47*) do not have sufficiently high resolution in the polar region to resolve the polar cap. More recent models (*48*), which include

MGS data when the spacecraft was at altitudes <200 km above the cap, also do not show a clear cap signature although smaller anomalies of the required magnitude are observed in the region. These results, if confirmed with additional data, would suggest that the northern cap is largely compensated and therefore relatively old compared with the time scale required for isostatic adjustment. For an upper mantle viscosity similar to that of Earth ($10^{21}$ Pa-s), the relaxation time for a load the size of the present cap is ~$10^5$ years (*49*), comparable to the time scales for periodicities in solar insolation that have been proposed to form laminae in the polar layered deposits (*3, 15*).

Although this result supports the view that the polar deposits are compensated, the form of the compensation will depend on the flexural rigidity of the martian lithosphere. Forward models of the loading of a spherical elastic shell by an axisymmetric polar cap (*50*), whose topographic profile approximates that of the northern cap of Mars, indicate that the base of the northern ice cap could extend from 500 to 1200 m beneath the level of the cap edge for elastic shell thicknesses of 40 to 200 km. The cap thickness is as much as 25% greater if the lithospheric shell supporting the ice cap is of low thickness (~40 km) and

rigidity than if the shell is as thick as 200 km.

Mantled plains (unit Hv in Fig. 1A) lie predominantly on shallow poleward facing slopes that descend to about 75°N and there are replaced by mantled smooth plains from about 60° to 275°E. The change in slope commonly seen at the boundary between these plains units supports the interpretation that the mantled plains underlie the mantled smooth plains and that deposits of the latter unit fill a circumpolar depression. This interpretation favors the presence of a thick elastic lithosphere ($T_e > 100$ km), which reduces the difference between the geometric and flexural estimates for the base of the ice cap. From the combined geometric and flexural volume limits we derive an equivalent mass of $1.4 \pm 0.3 \times 10^{18}$ kg of water for an assumed 100% $H_2O$ composition.

The MOLA north polar data appear to indicate that Mars now has less surficial water than it had in the past, which raises the question as to the fate of past water not currently present in the northern cap. Some of that water may be in the south polar cap, but that structure is considerably smaller than the northern cap and cannot likely account for the balance, even if it is composed almost entirely of $H_2O$. It has been suggested that the water currently resides in the regolith, recharged by basal melting of the northern cap (*17*). However, if the cap is composed of $H_2O$ then even in the limit of a thin lithosphere with maximum ice thickness the pressure at the base of the cap is insufficient for pressure melting to occur. For liquid water to be present, one or more constituents that lower the melting temperature, for example, salts, must be present in the cap. Alternatively, perhaps in past history the ice cap was sufficiently thick for basal melting to have occurred. Water can be lost by oxidation of
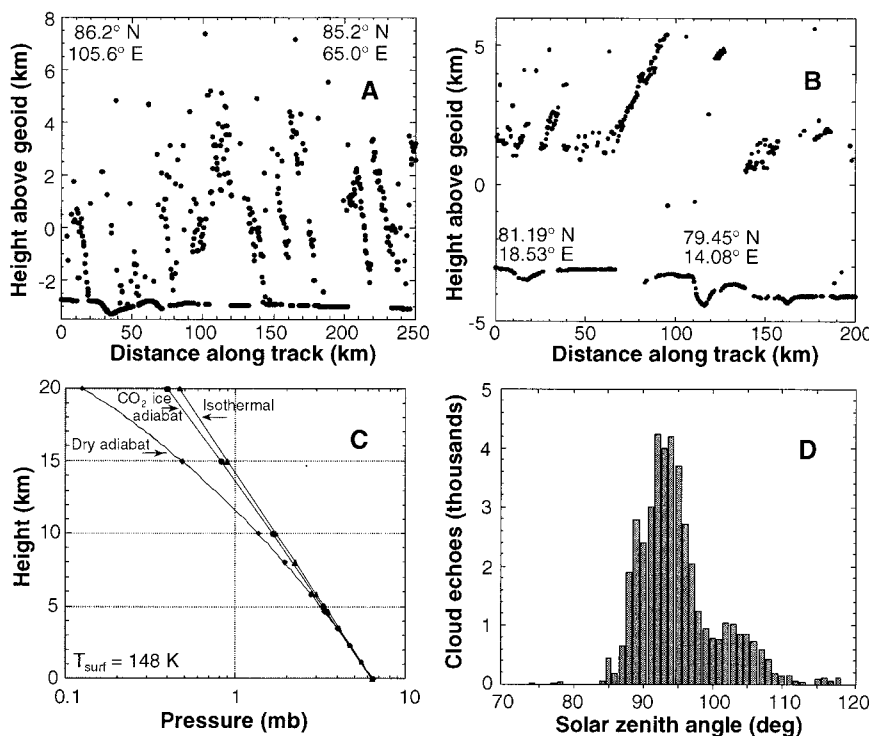


**Fig. 9. (A)** Sloping cloud features on Pass 260 that are believed to represent the phase fronts of gravity waves. **(B)** A sloping wavefront seen above a surface discontinuity on pass 332 that is thought to represent a stationary gravity or lee wave. In both (A) and (B) the polar vortex winds are blowing from right to left, and the nearly continuous line near the bottom corresponds to echoes from the surface. **(C)** Atmospheric pressure profiles for an isothermal ($L = 0$ K km$^{-1}$), a "wet" $CO_2$ adiabatic ($L = -0.85$ K km$^{-1}$), and a "dry" $CO_2$ adiabatic ($L = -4.3$ K km$^{-1}$) temperature lapse rate, $L$. **(D)** The distribution of observed cloud echoes from all passes in SPO as a function of solar zenith angle.

**Table 1.** Topographic characteristics of the Mars north polar region. Estimates of ice cap elevation and volume are shown with and without flexure (flex.) of the crust.

| Parameter | Value |
|---|---|
| *Planetary radii** | |
| Mean equator | $3396.0 \pm 0.3$ km |
| Top of northern icecap | $3376.24 \pm 0.05$ km |
| Base of ice cap, no flex., $c$ | $3373.3 \pm 0.2$ km |
| Equatorial axis, $a$ | $3399.5 \pm 0.3$ km |
| Equatorial axis, $b$ | $3392.5 \pm 0.3$ km |
| 1/flattening | $148.9 \pm 1.0$ |
| *Ice cap** | |
| Elevation of top | $-1950 \pm 50$ m |
| Elevation of base, no flex. | $-4900 \pm 200$ m |
| Thickness, no flex. | $2950 \pm 200$ m |
| Possible contrib. from flex. | 500 to 1200 m |
| Volume, no flex. | $1.2 \pm 0.2 \times 10^6$ km$^3$ |
| Volume, with flex. | 1.3 to $1.7 \times 10^6$ km$^3$ |
| Mass, $H_2O$ equivalent | $1.4 \pm 0.3 \times 10^{18}$ kg |
| Volume of dunes | $10 \pm 3 \times 10^3$ km$^3$ |

*Preliminary values.

surface rocks and exospheric escape of hydrogen. However, no current mechanisms can easily reconcile the current volume of surficial water with that which is believed to have existed early in Mars's history (42). A better understanding of the age of the ice cap and outliers would clarify the present-day sinks of $H_2O$ and the mechanisms of volatile loss.

**Obliquity**. The north polar radius measured to the top of the ice cap is $3376.24 \pm 0.05$ km (Table 1), which is 1 to 2 km less than that determined previously (10, 11). The north polar radius interpolated to beneath the ice cap (assuming no flexure) is $3373.3 \pm 0.2$ km. If uncompensated, the polar caps will contribute to the planet's mass distribution and modify the moment of inertia. If a cap of mass of $10^{18}$ kg were instantaneously removed, for example, as a result of melting during a period of astronomically forced high obliquity (3, 15), the ratio of the equatorial moments (A, B) of inertia of Mars to the polar moment of inertia (C) would change by a few parts in $10^6$, and the ratio of the difference in the moments of inertia [$C/(C - A)$] would change by a few parts in $10^3$. These changes are less than the present uncertainty in the moments of inertia (51) and will not significantly change Mars's rate or amplitude of axial precession. Thus, even rapid formation of the present-day north cap from volatiles and dust not originally near the pole would not destabilize Mars. A much larger cap, which could have existed in the past, would be needed to affect the long-term rotation of Mars. If the polar cap is of higher density due to inclusion of dust or other material, this balance will not be affected because the nonvolatile components would remain at the pole after sublimation of the water ice.

**Clouds**. Many (~50,000) laser returns from the tops of clouds were observed by MOLA during the SPOs, when observations were consistently made over the north polar caps. These orbits occurred near the time of expected maximum ice deposition during northern hemisphere winter (52), and clouds were seen on roughly 80% of the passes. Nearly all of the cloud detections were obtained over the north polar cap where the spacecraft passed below 400 km altitude (53).

Cloud tops varied from near the surface to altitudes of up to 15 km. Of particular interest are clouds with sloping tops that are assumed to mark the propagating phase fronts of gravity (or buoyancy) waves, as shown in Fig. 9, A and B. The image in Fig. 9A shows a series of sawtooth structures that extend from the surface up to 8 km. These structures are excited by turbulence associated either with the heat of fusion ($1.78 \times 10^5$ J kg$^{-1}$) released as atmospheric $CO_2$ condenses into dry ice in the winter polar caps (54) or with shear generated by the polar geostrophic winds (55). The clouds in Fig. 9B, on the

other hand, appear much like a lee wave (56), excited by the upward thrust of polar vortex winds as they strike a surface discontinuity.

A passing atmospheric wave makes a phase front visible when a volatile capable of condensing into reflecting particles and then evaporating is present, as perturbations in the ambient temperature of a few percent take place. In the winter polar caps, that volatile is almost certainly atmospheric $CO_2$. The existence of infrared-visible phase fronts suggests that the vertical temperature lapse rate of the winter polar cap atmosphere must follow that for a "wet" $CO_2$-ice adiabat, that is, $-0.85$ K km$^{-1}$ (Fig. 9C). Because a gravity wave requires a non-equilibrium restoring force from its surrounding medium, it cannot propagate in a truly adiabatic environment. We propose that, although the vertical temperature profile is in long-term equilibrium with the vapor pressure of $CO_2$ ice, in the absence of sufficient nucleation centers, the short-term fluctuations follow a "dry" $CO_2$ adiabat, corresponding to a lapse rate of $-4.3$ K km$^{-1}$ (Fig. 9C). Cloud returns observed by MOLA largely disappear as the sun rises above the horizon in the polar cap (Fig. 9D), probably because the atmosphere is quickly heated above that of a wet adiabat. Pressure data from the Viking landers (54) indicate that $CO_2$ condenses out of the atmosphere in martian polar regions in winter, and the MOLA observations suggest detection of these condensates.

**References and Notes**

1. P. Thomas, S. W. Squyres, K. Herkenhoff, A. Howard, B. Murray, in *Mars*, H. H. Kieffer, B. M. Jakosky, C. W. Snyder, M. S. Matthews, Eds. (Univ. of Ariz. Press, Tucson, 1992), pp. 767–795.
2. B. M. Jakosky and R. M. Haberle, in (1), pp. 969–1016.
3. F. P. Fanale, S. E. Postawko, J. B. Pollack, M. H. Carr, R. O. Pepin, in (1), pp. 1135–1179.
4. H. H. Kieffer and A. P. Zent, in (1), pp. 1180–1218.
5. M. T. Zuber *et al.*, *J. Geophys. Res.* **97**, 7781 (1992).
6. D. E. Smith *et al.*, *Science* **279**, 1686 (1998).
7. A. A. Albee, F. D. Palluconi, R. E. Arvidson, *ibid.*, p. 1671.
8. The MOLA instrument measures the round-trip time of flight of infrared (1.064-μm wavelength) laser pulses between the MGS spacecraft and the martian surface. The laser beam divergence of 400 μrad resulted in a surface spot size of 70 to 330 m along the spacecraft groundtrack (depending on spacecraft altitude), with a shot-to shot-spacing of ~400 m. By interpolating the spacecraft orbital trajectory to the time of the laser measurement, the one-way light time between the spacecraft and the surface was obtained. This time of flight was converted to range by dividing by the speed of light. MOLA range observations have a shot-to-shot precision of 37.5 cm (21).
9. Since insertion into a near-polar elliptical orbit around Mars, the MGS spacecraft has been progressively decreasing orbital eccentricity by aerobraking through the martian atmosphere during periapsis passes. Aerobraking decreases the spacecraft apoapsis altitude and is being utilized to achieve a circular 400-km mapping orbit. The MOLA instrument is able to obtain data only when the MGS spacecraft is not undergoing aerobraking passes, and then only at ranges less than 786 km, with the limit determined by the number of bits assigned to the range word. This range limit, as well as sensitivity, restricted topographic measurements to the

northern hemisphere of Mars within about $\pm 12$ minutes of periapsis.
10. D. Dzurisin and K. R. Blasius, *J. Geophys. Res.* **80**, 3286 (1975).
11. K. R. Blasius, J. A. Cutts, A. D. Howard, *Icarus* **50**, 140 (1982).
12. The MOLA polar grid was determined using a minimum-curvature spline-with-tension routine (60). On Mars 1° of latitude equals approximately 59 km.
13. Subtraction of the range from the MGS radial orbit yielded measurements of martian radius in a center of mass reference frame. The absolute accuracy of the elevations, which at present is 5 to 30 m (48, 61), is limited by the knowledge of the MGS orbits, which were determined using the NASA/GSFC GEODYN system of orbit-analysis programs (62), recently modified to utilize altimetry cross-overs to improve radial accuracy.

Topography is defined as the planetary radius minus the geoid, which is the planet's gravitational equipotential, here taken from the GMM-1 gravitational field model of Mars (46), and constrained to match Mars's revised mean equatorial radius ($3396.0 \pm 0.3$ km) (14). Otherwise, the current best IAU geophysical and coordinate system parameters (63) are used. Zero elevation is defined as the average radius of the geoid at the equator.
14. M. T. Zuber *et al.*, *Geophys. Res. Lett.*, in press.
15. O. B. Toon, J. B. Pollack, W. Ward, J. A. Burns, K. Bilski, *Icarus* **44**, 552 (1980).
16. F. P. Fanale, J. R. Salvail, A. P. Zent, S. E. Postawko, *ibid.* **67**, 1 (1986).
17. S. M. Clifford, *J. Geophys. Res.* **98**, 10,973 (1993).
18. The proposed aquifer is likely unconfined (corresponding to the water table), and the surface will follow a gravitational potential surface dictated by the hydrostatic head at the cap. To maintain energy balance, however, constant source flow would lead to a decrease in free surface (water table) elevation and an increase in specific discharge. The free surface at the equator will be beneath the planetary surface by an amount given by the pole-to-equator difference in surface elevation and the water table decrease due to energy balance. The proposed water table beneath the equator resulting from charging at the pole will be deeper than previously thought (17) because of the MOLA results. In addition, the bottom of the aquifer is controlled by the reduction of porosity (and thus permeability) to zero by lithostatic pressure. This bottom surface will approximately mimic the surface elevation and will cut off the aquifer as the elevation rises toward the equator unless the aquifer is sufficiently deep.
19. M. T. Zuber and D. E. Smith, *J. Geophys. Res.* **102**, 28,673 (1997).
20. M. C. Malin, unpublished data.
21. J. B. Abshire, X. Sun, R. S. Afzal, in preparation.
22. H. Tsoar, R. Greeley, A. R. Peterfreund, *J. Geophys. Res.* **84**, 8167 (1979).
23. A. D. Howard, J. A. Cutts, K. R. Blasius, *Icarus* **50**, 161 (1982).
24. D. A. Fisher, *ibid.* **105**, 501 (1993).
25. S. M. Clifford, *J. Geophys. Res.* **92**, 9135 (1987).
26. A. Howard, *TM 82385* (NASA, Greenbelt, MD, 1980).
27. R. Greeley, N. Lancaster, S. Lee, P. Thomas, in (1), pp. 730–766.
28. N. Lancaster and R. Greeley, *J. Geophys. Res.* **95**, 10,921 (1990).
29. H. H. Kieffer, S. C. J. Chase, T. Z. Martin, E. D. Miner, F. D. Palluconi, *Science* **194**, 1341 (1976).
30. B. M. Jakosky and C. B. Farmer, *J. Geophys. Res.* **87**, 2999 (1982).
31. D. O. Muhleman and A. B. Ivanov, in S. Clifford, D. Fisher, J. Rice, Eds., First International Conference on Mars Polar Science and Exploration, Camp Allen, TX (Lunar and Planetary Institute, Houston, 1998), pp. 28–29.
32. The loss rate of water from each point can be computed from the kinetic equation $dM/dt = -(P_{sat}(T) - P_w(t)) (m_w/2\pi kT)^{1/2}$, where $P_{sat}(T)$ is the temperature-dependent, saturation vapor pressure of water over ice, $P_w(t)$ is the time-dependent, partial pressure of the water vapor at the surface, and $m_w$ is the molecular weight of water. We assume that $P_w(t)$ is the surface partial pressure of uniformly mixed water

vapor that is consistent with the measured column abundances (64) as a function of seasons on Mars. Thus we neglect winds and other meteorological effects including water vapor diffusion through the $CO_2$ atmosphere. The primary effect of this approximation is to shorten the time scale of ablation by about an order of magnitude (30), which probably has little effect on the final cap shape, our major objective. The shape itself is mostly a consequence of the geometrical position of the sun relative to the ice cap. If we assume that the shape of the cap was initially like that of a hockey puck, best model fits were obtained with the albedo $A = 0.55$. During the season when the local point is not illuminated by the sun, the temperature was fixed at 150 K. The computations are made over a martian year and an obliquity equal to that of the current epoch was used.

33. W. B. Durham, S. H. Kirby, L. A. Stern, *J. Geophys. Res.* **102**, 16,293 (1997).
34. W. F. Budd, *J. Glaciol.* **9**, 29 (1970).
35. M. T. Zuber, L. Lim, H. J. Zwally, in (31), pp. 45–46.
36. R. Haefeli, *J. Glaciol.* **3**, 1133 (1961).
37. B. R. Clark and R. P. Mullin, *Icarus* **27**, 215 (1976); W. B. Durham, in (31), pp. 8–9.
38. W. B. Durham, S. H. Kirby, L. A. Stern, *J. Geophys. Res.* **97**, 20,883 (1992).
39. J. W. Head et al., *Geophys. Res. Lett.*, in press.
40. D. J. Drewry, S. R. Jordan, E. Jankowski, *Annals Glaciol.* **3**, 83 (1982).
41. To produce the geometric estimate for the volume of the north polar cap we first projected the polar topography using azimuthal equal area in the latitude range 70° to 90°N. We defined the outline of the polar cap on the basis of where the edge intersected the surrounding plain by comparison of MOLA topography with mapped geologic units (57, 65) as well as MOLA 1.064-$\mu$m surface reflectivity. We fit a degree-6 spherical harmonic surface to the plains outside the cap and subtracted this surface from the topography to produce a grid of residual topography. We then calculated the volume of the cap inside the outline above a zero contour of the residual grid. Our basal surface fits the floor of Chasma Boreale to $\pm50$ m. To test the sensitivity of the estimated volume to the degree-6 model of basal topography, we also fit cubic, quadratic, and degree-4 spherical harmonic surfaces. The calculated volumes were indistinguishable given the statistical confidence of the estimate.
42. M. H. Carr, *Water on Mars* (Oxford Univ. Press, New York, 1996).
43. T. J. Parker, D. S. Gorsline, R. S. Saunders, D. C. Pieri, D. M. Schneeberger, *J. Geophys. Res.* **98**, 11,061 (1993).
44. U. Radok et al., "Climatic and Physical Characteristics of the Greenland Ice Sheet" (CIRES, Univ. of Colorado, 1982).
45. H. J. Zwally, A. C. Brenner, J. A. Major, R. A. Bindschadler, J. G. Marsh, *Science* **246**, 1587 (1989).
46. D. E. Smith et al., *J. Geophys. Res.* **98**, 20,871 (1993).
47. A. S. Konopliv and W. L. Sjogren, "The JPL Mars Gravity Field, Mars50c, Based Upon Viking and Mariner 9 Doppler Tracking Data" (*Publ. 95–5*, Jet Propulsion Lab, Pasadena, CA, 1995).
48. D. E. Smith, M. T. Zuber, F. G. Lemoine, *Eos* **79**, F524 (1998); G. L. Tyler et al., ibid.
49. The relaxation time was determined from the solution for topographic expression of a surface load with wavelength $\lambda$ on a spherical planet consisting of an outer elastic shell that overlies a viscous interior (66). Models with elastic shell thicknesses of 0, 50, and 100 km yielded similar relaxation times, but different degrees of compensation in the asymptotic limit: 1, 0.7, and 0.5, respectively. For thick elastic lithospheres the load never relaxes completely because of support by membrane stresses.
50. H. Kraus, *Thin Elastic Shells* (Wiley, New York, 1967).
51. W. M. Folkner, C. F. Yoder, D. N. Yuan, E. M. Standish, R. A. Preston, *Science* **278**, 1749 (1997).
52. Calculations of expected ice deposition were based on simulations of atmosphere-cryosphere exchange performed by R. Haberle, personal communication.
53. For clouds to be detected by MOLA they must have a fairly sharp upper interface, with scattering particle densities in excess of a few per cubic centimeter over spatial scales of ~100 m. When echoes from this interface are too weak to exceed the MOLA detector's threshold, either because of too low a scattering particle density or because of excessive range, the later-arriving surface echo usually trips the system, and the cloud is not seen. Thus, a significant number of clouds were undoubtedly missed.
54. J. E. Tillman, *J. Geophys. Res.* **93**, 9433 (1988).
55. C. B. Leovy, *Adv. Space Res.* **2**, 19 (1982).
56. J. R. Holton, *An Introduction to Dynamic Meteorology*, ed. 3, (Academic Press, San Diego, 1992).
57. K. L. Tanaka, D. D. H. Scott, Map I-1802-C (U.S. Geological Survey, 1987).
58. P. Wessel, *Computers and Geosciences*, 333 (1989); P. Wessel and W. H. F. Smith, *Eos* **72**, 441 (Fall Suppl.) (1991).
59. J. B. Garvin and J. J. Frawley, *Geophys. Res. Lett.*, in press.
60. W. H. F. Smith and P. Wessel, *Geophysics* **55**, 293 (1990).
61. D. D. Rowlands, D. E. Pavlis, F. G. Lemoine, G. A. Neumann, S. B. Luthcke, in preparation.
62. D. D. Rowlands et al., "GEODYN II System Description" (Hughes-STX Contractor Report, 1993).
63. M. E. Davies et al., *Cel. Mech. and Dynam. Astron.* **63**, 127 (1996).
64. C. B. Farmer and P. E. Doms, *J. Geophys. Res.* **84**, 2881 (1979).
65. A. L. J. Dial (U.S. Geological Survey Misc. Inv. Series Map I-1640, 1984).
66. M. T. Zuber and S. Zhong, *Eos* **79**, F486 (1998).